

**Two-neutron transfer in  ${}^7\text{Be} + {}^9\text{Be}$  collisions**

U. Umbelino, K. C. C. Pires, R. Lichtenthaler, V. Scarduelli, G. A. Scotton, A. Lepine-Szily, and V. Guimaraes  
*Instituto de Fısica, Universidade de Sao Paulo, Sao Paulo 05508-090, SP, Brazil*

J. Lubian, B. Paes, and J. L. Ferreira  
*Instituto de Fısica, Universidade Federal Fluminense, Niteroi, Rio de Janeiro 24210-340, Brazil*

M. A. G. Alvarez  
*Departamento de Fısica Atomica Molecular y Nuclear (FAMN), Facultad de Fısica, Universidad de Sevilla, Sevilla 41102, Spain*

J. M. B. Shorto  
*Instituto de Pesquisas Energeticas e Nucleares (IPEN-CNEN), Sao Paulo, Brazil*

S. Appannababu  
*Department of Nuclear Physics, Andhra University, Visakhapatnam 530 003, India*

M. Assuncao  
*Departamento de Fısica, Universidade Federal de Sao Paulo, Campus Diadema, Sao Paulo 09913-030, SP, Brazil*

R. P. Condori  
*Departamento de Ciencias Naturales, Universidad Catolica San Pablo, Arequipa, Peru*

V. Morcelle  
*Departamento de Fısica, Universidade Federal Rural do Rio de Janeiro 23890-000, Brazil*

 (Received 19 September 2018; revised manuscript received 5 April 2019; published 26 June 2019)

Elastic scattering and transfer cross sections for the  ${}^7\text{Be} + {}^9\text{Be}$  system have been measured at  $E_{\text{lab}} = 23.1$  MeV using the  ${}^7\text{Be}$  radioactive secondary beam produced at Radioactive Ion Beams in Brazil facility at the University of Sao Paulo. The elastic scattering has been measured by detecting the  ${}^7\text{Be}$  scattered at forward angles in the laboratory system. The transfer reaction  ${}^9\text{Be}({}^7\text{Be}, {}^9\text{Be}){}^7\text{Be}$  was identified by detecting the  ${}^9\text{Be}$  scattered at the same laboratory angles. The elastic angular distribution has been analyzed by optical model calculations using a Woods-Saxon form factor whose parameters have been varied to best reproduce the experimental data at forward angles. Coupled reaction channels calculations (CRC) have been performed to describe the transfer, considering the coupling to the transfer channel and including contributions to the ground state and to the first excited state of  ${}^7\text{Be}(1/2^-; 429\text{ keV})$  in the final state. The spectroscopic amplitudes used in the CRC calculation have been derived from shell-model calculations. Similar CRC calculations were applied to existing  ${}^9\text{Be}(p, t){}^7\text{Be}$  data to check the consistency of our results for the  $({}^7\text{Be}, {}^9\text{Be})$  transfer reaction.

DOI: [10.1103/PhysRevC.99.064617](https://doi.org/10.1103/PhysRevC.99.064617)

**I. INTRODUCTION**

Transfer reactions are a powerful tool to explore the structure of the atomic nucleus. Nucleon transfer reaction measurements combined with a full quantum description of the reaction mechanism allow the determination of spectroscopic factors, which can be compared with those obtained from nuclear model calculations providing a bridge between direct reaction mechanism and nuclear structure. Two-nucleon transfers, in particular, are of great interest since they provide information about nucleon-nucleon correlations in nuclei [1]. The role of nucleon pairing has long been established in nuclear physics primarily by the determination of the binding

energies and the observation of their characteristic odd-even staggering [2,3]. The pairing force effect in the dynamics of a pair of nucleon transfers also has connection with important phenomena such as superfluidity [1] and in astrophysics mainly concerning neutron stars. Transfers induced by light particles such as  $(d, n)$ ,  $(d, p)$ ,  $({}^3\text{He}, d)$  and the transfer  $(t, p)$  and  $(p, t)$  reactions, among others, have been used extensively in the past to determine spectroscopic factors and to investigate the pairing force in nuclei [4–12]. Due to safety reasons, the  $(t, p)$  reactions have been substituted by  $({}^{18}\text{O}, {}^{16}\text{O})$  reaction [13–24] with the same goal, to study the effect of pairing correlations in transfer reactions.

Recently, the availability of secondary beams of unstable light nuclei opened a large field of new possibilities to study transfer reactions [25]. Unstable nuclei such as  ${}^6\text{He}$ ,  ${}^8\text{Li}$ ,  ${}^{11}\text{Li}$ ,  ${}^7\text{Be}$ ,  ${}^8\text{B}$ , and many others can now be used as probes in collisions with stable targets. New phenomena such as the neutron and proton halos have been observed in some of these (so-called) exotic nuclei, which, in many cases, present a pronounced clusterlike structure with very small separation energies. As a result, processes such as breakup or particle/cluster transfers can be greatly enhanced in reactions involving these projectiles. Studies of neutron transfers involving exotic nuclei have also proven beneficial in the field of nuclear astrophysics. The synthesis of elements in stars, such as the  $r$  and  $s$  processes, take place via a sequence of neutron capture reactions and the presence of neutron- and proton-rich nuclei in the primordial nucleosynthesis scenario could open new paths to the overcome the  $A = 5, 8$  gaps all the way through to the formation of heavy elements.

The type of transfer reaction that draws a great interest is the so-called elastic transfer process [13,18,26,27]. In general, in the collision of two nuclei at low energies, elastic scattering and fusion are the dominating processes concerning the magnitude of the cross sections. However, if the projectile and target differ by only one valence particle or a cluster attached to the same core, there is also the possibility of an exchange of this valence particle between the two cores, giving rise to an exchange of identity between projectile and target, and leading to the same entrance channel. If the exit and entrance channels are identical, the reaction  $Q$  value of this process is zero, which, due to favorable matching conditions, enhances the neutron transfer probability. In this kind of process, the elastic and the transfer amplitudes are entangled, making it difficult to separate the two processes. However, in some cases, it is possible to separate the two processes experimentally, by performing measurements at different angular ranges, where each amplitude dominates. It has been demonstrated that, when energies are not too low, the elastic scattering dominates the forward angles whereas the transfer amplitude dominates at backward angles [13,26,28].

In this paper, we present measurements of the  ${}^7\text{Be} + {}^9\text{Be}$  collision, with  $E_{\text{lab}} = 23.1$  MeV, at forward and backward angles in the center of mass system. A rise of the cross section at backward angles was observed indicating that the elastic transfer process plays a role. We analyze the data considering the effect of the transfer process on the elastic scattering. A full coupled reaction channels (CRC) calculation has been performed considering the coupling to the two-neutron transfer channel. All the spectroscopic amplitudes of the two-neutron cluster on the  ${}^7\text{Be}$  core have been calculated independently from the nuclear structure model and used in the CRC calculation.

This paper is organized as follows. The experimental setup is described in Sec. II. Section III is devoted to the comparison of theoretical results with the experimental angular distributions. In Sec. IV we used the same methodology used for the ( ${}^7\text{Be}$ ,  ${}^9\text{Be}$ ) reaction to calculate ( $p$ ,  $t$ ) reaction, and compare with the data available in the literature. Finally, the main conclusions are reported in Sec. V.

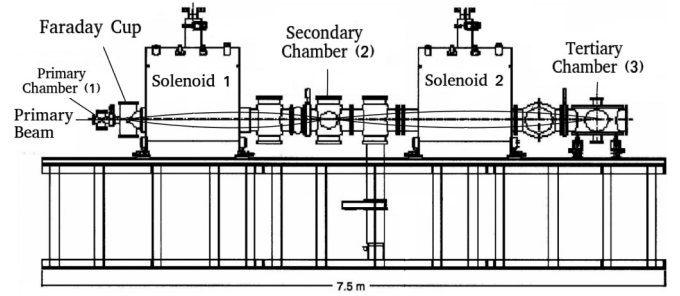


FIG. 1. RIBRAS scheme.

## II. EXPERIMENTAL SETUP AND RESULTS

The measurements have been performed in the Radioactive Ion Beams in Brazil (RIBRAS) facility [29,30] at the University of São Paulo. Figure 1 shows the diagram of the RIBRAS system. It consists of two superconducting solenoids and a sequence of three scattering chambers: (i) primary chamber where the radioactive  ${}^7\text{Be}$  beam was produced; (ii) secondary chamber located after the first solenoid, and (iii) tertiary chamber mounted after the second solenoid. The present experiment was performed in the secondary chamber using only the first solenoid as selector.

The 30 MeV  ${}^6\text{Li}^{3+}$  primary beam was provided by the 8-UD Pelletron accelerator with an intensity of 200–300 nAe. The  ${}^7\text{Be}$  secondary beam was produced by the proton transfer reaction  ${}^7\text{Li}({}^6\text{Li}, {}^7\text{Be})$  ( $Q = -4.37$  MeV) using a LiF primary target of thickness  $454 \mu\text{g}/\text{cm}^2$ . The primary beam was suppressed by a Faraday Cup placed at zero degrees just after the primary target. The Faraday cup current is measured and integrated to provide a measurement of the total number of primary beam particles incident during the run. The secondary  ${}^7\text{Be}$  beam is selected by the first solenoid (in the angular range  $2^\circ$ – $6^\circ$ ) and focused in the second scattering chamber. During the experiment, the intensity of the  ${}^7\text{Be}$  secondary beam was of the order of  $5 \times 10^4$  pps. Two secondary targets were mounted in the secondary chamber, a  ${}^9\text{Be}$  ( $1.92 \text{ mg}/\text{cm}^2$ ) and a  ${}^{197}\text{Au}$  ( $4.6 \text{ mg}/\text{cm}^2$ ). The  ${}^{197}\text{Au}$  target was used to normalize the cross sections since the  ${}^7\text{Be} + {}^{197}\text{Au}$  scattering is pure Rutherford in the energy and angular range of this experiment. Two Silicon Surface Barriers telescopes [ $\Delta E(25 \mu\text{m})$ – $E(1000 \mu\text{m})$ ] with an opening of 20 msr solid angle were mounted in the rotating plate to perform the measurements in the angular range from  $15^\circ$ – $48^\circ$  in the laboratory. The  $\Delta E$ - $E$  telescopes provided a good mass ( $A$ ) and charge ( $Z$ ) identification allowing to separate the  ${}^7\text{Be}$  particles from other contaminants present in the secondary beam (see Fig. 2). An energy calibration was done using a  ${}^{241}\text{Am}$   $\alpha$  source, and the residual energy  $E$  was summed to  $\Delta E$  to obtain the total energy.

Figure 2 shows a  $\Delta E$ - $E$  spectrum of the secondary beam scattered at  $15^\circ$  in the gold target. We clearly identify the peak corresponding to the  ${}^7\text{Be}$  secondary beam scattered in the gold target, well separated from the contaminants. Usual contaminants are the energy degraded  ${}^6\text{Li}$  particles coming from the primary beam and light particles ( $\alpha$ , protons, deuterons, and tritons) produced in reactions in the primary target. In the

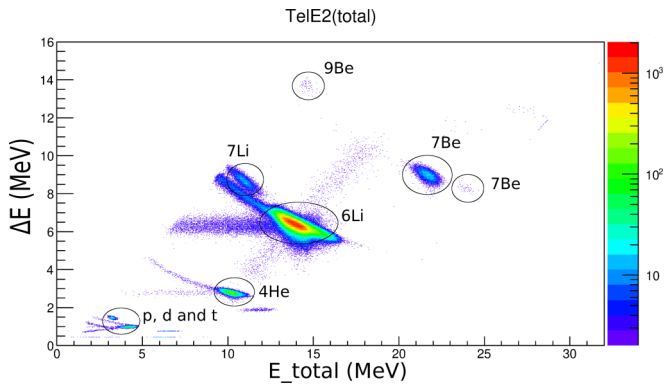


FIG. 2.  $\Delta E$ - $E_{\text{total}}$  spectrum obtained at  $\theta_{\text{lab}} = 15^\circ$  with gold target.

lithium line we observe a low-energy peak of  ${}^7\text{Li}$  particles coming from the primary target and well separated from the  ${}^6\text{Li}$ , showing our good mass resolution. In the berillium line we observe two less intense peaks, one at higher energies corresponding to  ${}^7\text{Be}$  particles coming from the  ${}^{19}\text{F}({}^6\text{Li}, {}^7\text{Be})$  reaction and another at very low energies, near to the  $\Delta E$  threshold. All the intense peaks observed in Fig. 2 correspond to particles produced in the primary target, which are coming in the cocktail beam. Due to the low energies, the Coulomb barrier practically prevents nuclear reactions in the gold target.

In Fig. 3, we observe the same spectrum but scattered in the  ${}^9\text{Be}$  target. Again, the resolution was largely sufficient to identify the  ${}^7\text{Be}$  peak as well as all the other contaminants as in the case of the gold target. We note that there are many more  $\alpha$ s and light particles than in the gold target spectrum, due to nuclear reactions between the secondary beam particles and the  ${}^9\text{Be}$  target, as the energy of the secondary beam is several times above the  ${}^9\text{Be}$  Coulomb barrier.

Above the  ${}^7\text{Be}$  line, one can observe a group of particles in the  ${}^9\text{Be}$  line. The energies of these particles match the energy expected for the recoil  ${}^9\text{Be}$  from the  ${}^9\text{Be}({}^7\text{Be}, {}^9\text{Be})$  reaction and mainly, these particles are not seen in the gold target spectrum, showing that they are not coming with secondary beam but are produced in the secondary target. As the  ${}^9\text{Be}$  recoil particles, detected at forward angles (in the laboratory), provide information of the  ${}^7\text{Be} + {}^9\text{Be}$  cross sections at backward angles in the center of mass system one is able

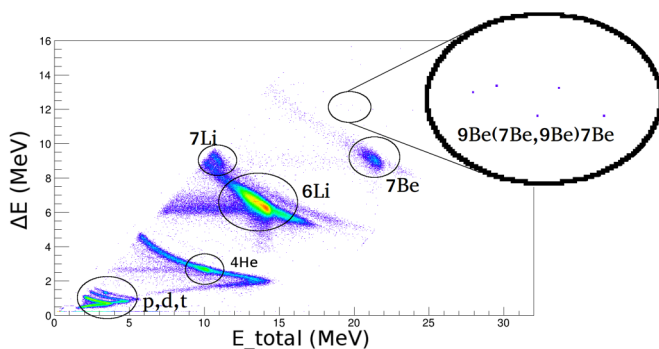


FIG. 3.  $\Delta E$ - $E_{\text{total}}$  spectrum obtained at  $\theta_{\text{lab}} = 15^\circ$  with beryllium target.

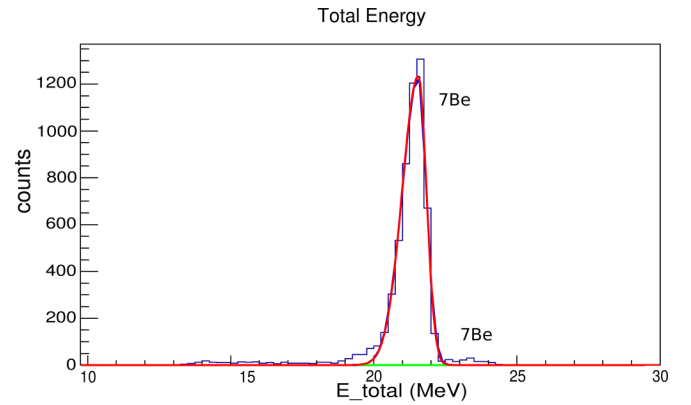


FIG. 4. Energy spectrum obtained at  $\theta_{\text{lab}} = 15^\circ$  with beryllium target.

to simultaneously obtain both cross sections at forward and backwards angles in the center of mass system.

A total energy spectrum of the Beryllium line is presented in Fig. 4. The energy resolution of the  ${}^7\text{Be}$  beam ( $E_{FWHM} \approx 0.9$  MeV) is not sufficient to separate the contribution of the low-lying  ${}^7\text{Be}_{0.43}$  excited state and this effect will be properly treated in the analysis presented in the next sections. The energy resolution of the secondary beam is determined by two effects: the energy straggling in the primary target ( $\approx 340$  keV) and the kinematic broadening due to the angular acceptance of the solenoid ( $2 \leq \theta \leq 6^\circ$ ). The energy straggling is caused by the differential energy loss of the secondary particles when the production reaction occurs either in the beginning or in the end of the secondary target foil. The contribution of the primary beam to the final energy resolution is negligible.

To monitor the  ${}^7\text{Be}$  production rate during the experiment and obtain the absolute cross sections, we performed runs with a  ${}^{197}\text{Au}$  target just before and after each  ${}^9\text{Be}$  run. The  ${}^7\text{Be} + {}^9\text{Be}$  elastic cross section was then determined using the expression below:

$$\sigma_{7\text{Be}+{}^9\text{Be}} = \sigma_{7\text{Be}+{}^{197}\text{Au}} \frac{N_c^{\text{Be}} J^{\text{Be}} N_b^{\text{Au}} N_t^{\text{Au}}}{N_c^{\text{Au}} J^{\text{Au}} N_b^{\text{Be}} N_t^{\text{Be}}}, \quad (1)$$

where  $N_c$  is the count number recorded at the interest peak,  $N_t$  is the target thickness (in atoms/cm<sup>2</sup>),  $J$  is the Jacobian of the transformation from the laboratory to center-of-mass frame, and  $N_b^{\text{Au}}/N_b^{\text{Be}}$  is the ratio of the number of  ${}^7\text{Be}$  particles incident in the Au and Be targets. This was taken as the ratio of the primary beam Faraday Cup integrator, assuming that the  ${}^7\text{Be}$  production is proportional to the primary beam intensity. The resulting angular distribution, including both forward and backward angles, is shown in Fig. 8 and the errors are purely statistical.

### III. THEORETICAL ANALYSIS

#### A. Brief theoretical description

The theoretical analysis of the  ${}^7\text{Be}({}^9\text{Be}, {}^7\text{Be}){}^9\text{Be}$  reaction was done by the coupled reaction channels (CRC) method. The coupling scheme considered in the calculations is shown

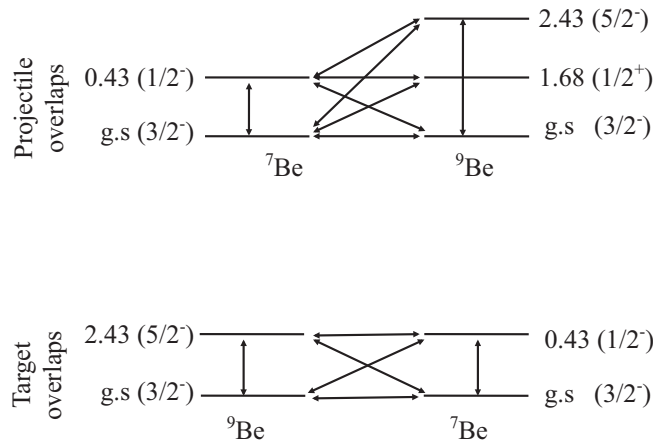


FIG. 5. Coupling schemes considered in the two-neutron transfer calculation.

in Fig. 5. All calculations were performed using the FRESKO [31] code. The São Paulo double folding potential [32] was used in both real and imaginary parts of the optical potentials of the entrance and outgoing partitions. In the entrance partition, a strength factor 0.6 was used for both real and imaginary parts. The use of this factor is justified as taking into account the missing couplings to dissipative processes [33], as well as, for the coupling to the continuum states that were not explicitly included in the coupling scheme [34]. In this last work, Sakuragi *et al.* showed that to fit the elastic scattering angular distributions of the  ${}^6\text{Li} + {}^{28}\text{Si}$  system, using double folding potentials for both real and imaginary parts, the strength coefficient of each part has to be set equal to 0.6. These results have been obtained from other systems involving other weakly bound systems (see Refs. [35,36] and references therein). Nevertheless, when verifying the sensitivity of our results regarding changes of these strength coefficients between 0.5 and 0.7 only showed a slight change of less than 5%.

Besides that, Fernández-García *et al.* [37], has shown the relevance of the couplings with the continuum states in the entrance partition as well as the relevance of the transfer for the continuum states in the final partition to describe the elastic scattering angular distribution in the  ${}^{11}\text{Li} + {}^{208}\text{Pb}$  reaction, where the weakly bound nucleus is considered as projectile. By comparing the theoretical energy distribution of the outgoing  ${}^9\text{Li}$  fragments with the experimental data in that reaction, the authors show that at forward angles the direct breakup is the most relevant process when compared with the one- and two-neutron transfer mechanisms, while the transfer become the most important process at backward angles and when the bombarding energy increases. This suggests that special attention should be given to the role of the couplings with the continuum states when weakly bound nuclei are involved in the reaction. The couplings with the continuum states have also shown to be relevant to describe the elastic scattering of the Borromean nucleus  ${}^6\text{He}$  on the different targets [38].

In the outgoing partition, the real and imaginary parts of the potential were multiplied by strength coefficients

$N_R = 1.0$  and  $N_I = 0.78$  respectively, as no couplings were explicitly considered [39,40]. The reduced electric transition probabilities for the collective excitation of the  ${}^7\text{Be}$  nucleus were obtained from Ref. [41]. They were used to derive the coupling matrix elements between projectile bound states. The transition form factors for collective excitations were considered as the derivative of the real part of the optical potential, as per usual. The full complex remnant couplings, prior representation of the optical potentials and nonorthogonality corrections were adopted to coupling the two mass partitions although it is important to note that, for the elastic-transfer case, the overlaps in the initial and final states are the same, which makes prior and post representations exactly the same, simplifying the description.

Single-particle wave functions were generated by using a Woods-Saxon potential, and the two-neutron wave functions were built by coupling two single-particle wave functions, as follows:

$$\begin{aligned} \phi_I(\xi_c, \mathbf{r}_1, \mathbf{r}_2) \\ = \sum_{l_s j} A_{l_s j}^{j_l, I} [\phi_{l_c}(\xi_c) \otimes [\phi_{l_1 s_1 j_1}(\mathbf{r}_1) \otimes \phi_{l_2 s_2 j_2}(\mathbf{r}_2)]_{l_s j}]_I, \end{aligned} \quad (2)$$

where  $\phi_{l_1 s_1 j_1}(\mathbf{r}_1)$  and  $\phi_{l_2 s_2 j_2}(\mathbf{r}_2)$  are the single-particle wave functions, which are coupled to give the two-neutron wave function and then coupled to the core wave function,  $\phi_{l_c}$ , to obtain the wave function of the nucleus composed by core plus two valence neutrons.  $A_{l_s j}^{j_l, I}$  represents the spectroscopic amplitude corresponding to the two-neutron valence configuration. In (2)  $l_i, s_i, j_i$  stand for the orbital, spin and total angular momentum, while  $l_c$  and  $I$  for the spin of the core and the total spin of the nucleus.

The two-neutron transfer reaction can be analyzed in two different ways, with a direct (simultaneous) or two-step mechanisms. The former is related to the two neutrons simultaneously transferred and to carry out the transfer calculations, the cluster and independent coordinates (IC) models can be used [13–24]. The latter, which is also called sequential transfer, corresponds to the two neutrons transferred in sequence passing through an intermediate partition. In fact, to consider a full quantum treatment of the two-nucleon transfer process both mechanisms should be considered together in the same calculation because they could produce interference with each other. However, in order to probe the single- or two-particle nature of the final states populated by the two transferred nucleons, it is important to take into account separately each mechanism.

In the two-neutron sequential transfer calculation, to fit the experimental one-neutron binding energies the depth of the Woods-Saxon potential was varied. On the other hand, as a common procedure in the independent coordinates two-neutron direct transfer [42], the bound-state potential for each valence single particle is adjusted to reproduce the half of the two-neutron binding energy.

The radius concerning the distance from the core ( ${}^7\text{Be}$ ) to the single valence neutrons was considered as the same one connecting the core to the center-of-mass of the two valence neutrons in which it has been calculated by using  $R = r_0(A_{7\text{Be}}^{1/3} + A_{2n}^{1/3})$  ( $r_0 = 1.25$  fm), where the mass of the

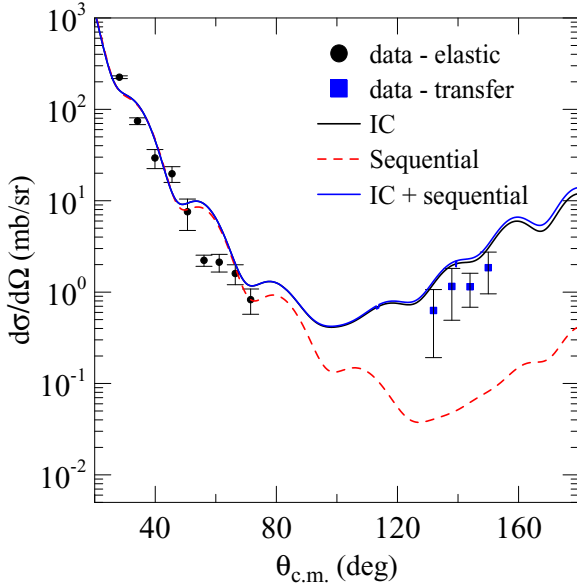


FIG. 6. Comparison of theoretical CRC predictions for the angular distribution of the direct and sequential transfer using the São Paulo potential as an optical potential in both partitions, with the experimental data.

two neutrons was taken into account. From this procedure, the r.m.s radius equal to 3.44 fm was obtained for the single neutron outside the core. This value is in agreement with the r.m.s radius (3.53 fm) for the valence neutron in  ${}^9\text{Be}$  nucleus obtained by Rocca and Iachello [43]. In this work, the authors described the structure of the  ${}^9\text{B}$  and  ${}^9\text{Be}$  nuclei using the cluster shell model [44]. Alternatively, one could use only the mass of the core to define the radius of the potential that binds each neutron. In this case, a reduced radius of 1.98 fm is necessary to obtain the same r.m.s radius of the  ${}^9\text{Be}$  in its ground state. It is important to mention that the same radius was used to bind the neutrons in the direct and sequential transfer mechanisms.

In this work, as it will be shown in Fig. 6, the direct mechanism is dominant, and it is about one order of magnitude higher than the sequential mechanism. In that figure, the angular distributions concerning the direct and direct+sequential transfers are almost indistinguishable. The coupling scheme considered in the sequential calculation is shown in Fig. 7 and the spectroscopic amplitudes used in this calculation can be observed in Table I.

In the independent coordinates model, the single-particle states of the two neutrons outside of the core are used to build the two-neutron wave functions with their respective spectroscopic amplitudes. Then, a coordinate transformation is performed from the relative movement of each neutron to the core into the coordinate of their center-of-mass related to the core and their relative motion coordinate. This picture allows us to analyze the importance of intrinsic states of the system formed by the two neutrons.

To perform CRC calculation microscopically, it is necessary to calculate the spectroscopic amplitudes concerning the projectile and target overlaps. In the present case, these

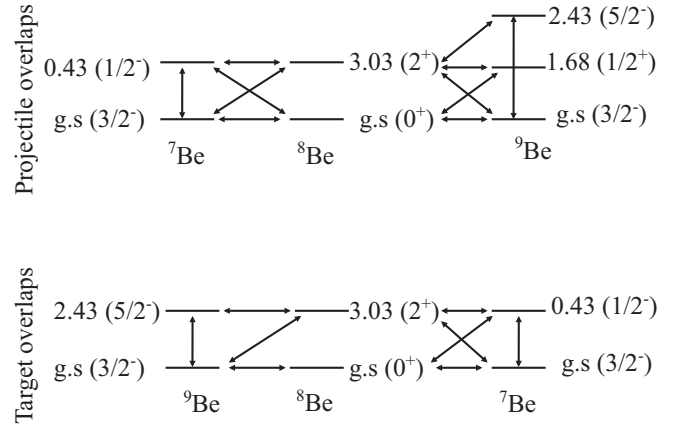


FIG. 7. Coupling schemes considered in the sequential transfer calculation.

spectroscopic amplitudes were obtained by performing shell-model calculations using the NUSHELLX code [45]. To obtain one- and two-neutron spectroscopic information related to the projectile and target overlaps, the structure model *psdpn*, which takes the *p* and *sd* shells as valence subspace for both protons and neutrons and the effective phenomenological *psdmod* interaction [46], were considered. In principle, to describe the low-lying states of the  ${}^{7,9}\text{Be}$  nuclei with negative parity the *p* shell might be enough as the most significant contribution comes from the orbits inside this shell, as can be observed from Table II, where the spectroscopic amplitudes for the projectile and the target overlaps are shown. On the other hand, the  ${}^9\text{Be}$  nucleus has a positive parity low-lying state that can only be described if the model space is increased. For this reason, the *psdmod* interaction was considered to describe the structures of the  ${}^{7,8,9}\text{Be}$  isotopes.

In Table III, the theoretical spectra obtained using the NUSHELLX code are compared with the experimental values [47] for all the nuclei involved in the reaction. In Table IV the

TABLE I. Spectroscopic amplitudes used in the CRC calculations for the sequential transfer reactions, where  $j_1 j_2$  are the spins of the neutron orbitals for the sequential transfer.

Initial State	$j_1 j_2$	Final State	Spect. Ampl.
${}^7\text{Be}_{g.s.}(3/2^-)$	$(1p_{3/2})$	${}^8\text{Be}_{g.s.}(0^+)$	-1.202
${}^7\text{Be}_{0.43}(1/2^-)$	$(1p_{1/2})$	${}^8\text{Be}_{g.s.}(0^+)$	-0.686
${}^7\text{Be}_{g.s.}(3/2^-)$	$(1p_{1/2})$ $(1p_{3/2})$	${}^8\text{Be}_{3.03}(2^+)$	0.571 0.771
${}^7\text{Be}_{0.43}(1/2^-)$	$(1p_{3/2})$	${}^8\text{Be}_{3.03}(2^+)$	-0.655
${}^8\text{Be}_{g.s.}(0^+)$	$(1p_{3/2})$	${}^9\text{Be}_{g.s.}(3/2^-)$	-0.743
${}^8\text{Be}_{3.03}(2^+)$	$(1p_{1/2})$ $(1p_{3/2})$	${}^9\text{Be}_{g.s.}(3/2^-)$	0.173 -0.866
${}^8\text{Be}_{g.s.}(0^+)$	$(2s_{1/2})$	${}^9\text{Be}_{1.68}(1/2^+)$	-0.694
${}^8\text{Be}_{3.03}(2^+)$	$(1d_{3/2})$ $(1d_{5/2})$	${}^9\text{Be}_{1.68}(1/2^+)$	-0.107 0.667
${}^8\text{Be}_{3.03}(2^+)$	$(1p_{1/2})$ $(1p_{3/2})$	${}^9\text{Be}_{2.43}(5/2^-)$	-0.342 0.954

TABLE II. Spectroscopic amplitudes used in the CRC calculations for two-neutron transfer reactions, where  $j_1 j_2$  are the spins of the neutron orbitals for two-neutron transfer, and  $J_{12}$  is the angular momentum of the two-neutron system.

Initial State	$j_1 j_2$	$J_{12}$	Final State	Spect. Ampl.
${}^7\text{Be}_{g.s.}(3/2^-)$	$(1p_{3/2})^2$	0.0	${}^9\text{Be}_{g.s.}(3/2^-)$	0.267
	$(1p_{1/2})^2$			0.174
	$(1d_{5/2})^2$			0.014
	$(1d_{3/2})^2$			0.010
	$(2s_{1/2})^2$			0.004
${}^7\text{Be}_{g.s.}(3/2^-)$	$(1p_{3/2})^2$	2.0	${}^9\text{Be}_{g.s.}(3/2^-)$	-1.259
	$(1p_{3/2}1p_{1/2})$			-0.035
	$(1d_{5/2})^2$			0.001
	$(1d_{5/2}1d_{3/2})$			-0.005
	$(1d_{5/2}2s_{1/2})$			-0.006
	$(1d_{3/2})^2$			-0.004
	$(1d_{3/2}2s_{1/2})$			-0.011
${}^7\text{Be}_{g.s.}(3/2^-)$	$(1p_{3/2}1d_{5/2})$	1.0	${}^9\text{Be}_{1.68}(1/2^+)$	0.163
	$(1p_{3/2}1d_{3/2})$			-0.066
	$(1p_{3/2}2s_{1/2})$			0.549
	$(1p_{1/2}1d_{3/2})$			0.063
	$(1p_{1/2}2s_{1/2})$			0.058
${}^7\text{Be}_{g.s.}(3/2^-)$	$(1p_{3/2}1d_{5/2})$	2.0	${}^9\text{Be}_{1.68}(1/2^+)$	0.536
	$(1p_{3/2}1d_{3/2})$			0.031
	$(1p_{3/2}2s_{1/2})$			0.719
	$(1p_{1/2}1d_{3/2})$			-0.403
	$(1p_{1/2}2s_{1/2})$			-0.033
${}^7\text{Be}_{g.s.}(3/2^-)$	$(1p_{3/2}1p_{1/2})$	1.0	${}^9\text{Be}_{2.43}(5/2^-)$	-0.352
	$(1d_{5/2}1d_{3/2})$			-0.004
	$(1d_{3/2}2s_{1/2})$			-0.010
	$(1p_{3/2})^2$			-0.292
	$(1p_{3/2}1p_{1/2})$			-0.620
${}^7\text{Be}_{g.s.}(3/2^-)$	$(1d_{5/2})^2$	2.0	${}^9\text{Be}_{2.43}(5/2^-)$	0.026
	$(1d_{5/2}1d_{3/2})$			-0.026
	$(1d_{5/2}2s_{1/2})$			0.015
	$(1d_{3/2})^2$			0.010
	$(1d_{3/2}2s_{1/2})$			0.013
${}^7\text{Be}_{0.429}(1/2^-)$	$(1p_{3/2}1p_{1/2})$	1.0	${}^9\text{Be}_{g.s.}(3/2^-)$	0.331
	$(1p_{1/2}1d_{5/2})$			0.001
	$(1d_{3/2}2s_{1/2})$			0.002
${}^7\text{Be}_{0.429}(1/2^-)$	$(1p_{3/2})^2$	2.0	${}^9\text{Be}_{g.s.}(3/2^-)$	0.216
	$(1p_{3/2}1p_{1/2})$			0.382
	$(1d_{5/2})^2$			-0.009
	$(1d_{5/2}1d_{3/2})$			0.006
	$(1d_{5/2}2s_{1/2})$			-0.003
${}^7\text{Be}_{0.429}(1/2^-)$	$(1d_{3/2})^2$	0.0	${}^9\text{Be}_{1.68}(1/2^+)$	0.002
	$(1d_{3/2}2s_{1/2})$			-0.004
	$(1p_{3/2}1d_{3/2})$			-0.092
	$(1p_{1/2}2s_{1/2})$			0.210
	$(1p_{3/2}1d_{5/2})$			0.442
${}^7\text{Be}_{0.429}(1/2^-)$	$(1p_{3/2}1d_{3/2})$	1.0	${}^9\text{Be}_{1.68}(1/2^+)$	0.040
	$(1p_{3/2}2s_{1/2})$			-0.044
	$(1p_{1/2}1d_{3/2})$			0.005
	$(1p_{1/2}2s_{1/2})$			0.361

TABLE II. (*Continued.*)

Initial State	$j_1 j_2$	$J_{12}$	Final State	Spect. Ampl.
${}^7\text{Be}_{0.429}(1/2^-)$	$(1p_{3/2})^2$	2.0	${}^9\text{Be}_{2.43}(5/2^-)$	-0.805
	$(1p_{3/2}1p_{1/2})$			-0.058
	$(1d_{5/2})^2$			0.009
	$(1d_{5/2}1d_{3/2})$			0.003
	$(1d_{5/2}2s_{1/2})$			0.007
	$(1d_{3/2})^2$			-0.002
	$(1d_{3/2}2s_{1/2})$			-0.001

theoretical magnetic and electric multipole reduced transition probabilities are compared with experimental data [47], upon availability. The theoretical multipole magnetic and electric moments are also shown in this table. Despite the fact that the  ${}^9\text{Be}$  nucleus has a known cluster structure, in which its properties have been reproduced by considering the  $\alpha + \alpha + n$  configuration [48–50], from these two tables, it is observed that a reasonably good agreement between the theory and the experiment was achieved, allowing the same confidence regarding the structural characteristics derived for these nuclei.

In principle, to calculate the angular distribution for the  ${}^7\text{Be}({}^9\text{Be}, {}^7\text{Be}_{gs}){}^9\text{Be}_{gs}$  system, which involves identical initial and final partitions, we should carry out the coherent sum of

TABLE III. Comparison between theoretical and experimental spectra of the  ${}^{7,8,9}\text{Be}$  isotopes.

${}^7\text{Be}$				
Exp.		Theo.		$ \Delta E $ (MeV)
$E$ (MeV)	$I^\pi$	$E$ (MeV)	$I^\pi$	
0.0	$3/2^-$	0.0	$3/2^-$	0
0.429	$1/2^-$	0.964	$1/2^-$	0.54
4.571	$7/2^-$	4.803	$7/2^-$	0.23
6.730	$5/2^-$	6.489	$5/2^-$	0.24
7.211	$5/2^-$	7.729	$5/2^-$	0.52
${}^8\text{Be}$				
Exp.		Theo.		$ \Delta E $ (MeV)
$E$ (MeV)	$I^\pi$	$E$ (MeV)	$I^\pi$	
0.0	$0^+$	0.0	$0^+$	0
3.030	$2^+$	3.527	$2^+$	0.50
11.350	$4^+$	11.001	$4^+$	0.35
${}^9\text{Be}$				
Exp.		Theo.		$ \Delta E $ (MeV)
$E$ (MeV)	$I^\pi$	$E$ (MeV)	$I^\pi$	
0.0	$3/2^-$	0.0	$3/2^-$	0
1.684	$1/2^+$	1.845	$1/2^+$	0.16
2.429	$5/2^-$	2.843	$5/2^-$	0.41
2.780	$1/2^-$	3.514	$1/2^-$	0.73
3.050	$5/2^+$	2.353	$5/2^+$	0.70

TABLE IV. Comparison between theoretical and experimental multipole magnetic and electric reduced transition amplitudes between different states and magnetic and electric multipole moments of the  ${}^{7,8,9}\text{Be}$  isotopes.

${}^7\text{Be}$			
	$I^\pi$	Exp.	Theo.
$Q(\text{efm}^2)$	$3/2_1^-$		-4.88
$\mu(\mu N)$	$3/2_1^-$		-1.348
$E$ (MeV)	$I_i^\pi \rightarrow I_f^\pi$	Exp.(W.u.)	Theo.(W.u.)
$B(M1)$	$1/2_1^- \rightarrow 3/2_1^-$	$2.07 \pm 0.27$	5.711
	$5/2_1^- \rightarrow 3/2_1^-$		0.001
	$5/2_1^- \rightarrow 7/2_1^-$		5.258
$B(E2)$	$1/2_1^- \rightarrow 3/2_1^-$		20.220
	$7/2_1^- \rightarrow 3/2_1^-$		9.344
	$5/2_1^- \rightarrow 1/2_1^-$		6.290
	$5/2_1^- \rightarrow 3/2_1^-$		2.242
	$5/2_1^- \rightarrow 7/2_1^-$		2.992
${}^8\text{Be}$			
	$I^\pi$	Exp.	Theo.
$Q(\text{efm}^2)$	$2_1^+$		-7.820
$\mu(\mu N)$	$2_1^+$		1.015
$E$ (MeV)	$I_i^\pi \rightarrow I_f^\pi$	Exp.(W.u.)	Theo.(W.u.)
$B(E2)$	$2_1^+ \rightarrow 0_1^+$		13.620
	$4_1^+ \rightarrow 2_1^+$		11.800
${}^9\text{Be}$			
	$I^\pi$	Exp.	Theo.
$Q(\text{efm}^2)$	$3/2_1^-$	$5.3 \pm 0.3$	4.870
$\mu(\mu N)$	$3/2_1^-$	-1.178	-1.176
$E$ (MeV)	$I_i^\pi \rightarrow I_f^\pi$	Exp.(W.u.)	Theo.(W.u.)
$B(M1)$	$5/2_1^- \rightarrow 3/2_1^-$	$0.30 \pm 0.03$	0.853
	$1/2_1^- \rightarrow 3/2_1^-$		3.571
$B(E2)$	$5/2_1^- \rightarrow 3/2_1^-$	$24.4 \pm 1.8$	24.220
	$1/2_1^- \rightarrow 3/2_1^-$		0.021
	$1/2_1^- \rightarrow 5/2_1^-$		5.330

the elastic scattering and elastic transfer amplitudes as they are indistinguishable from one another. On the other hand, in some works involving reactions with identical initial and final partitions, the experimental data at backward angles has been associated with the transfer channel at forward angles, and the theoretical results could successfully be reproduced [13,51]. Indeed, it is possible to predict the angular range in which the interference effect among the elastic scattering and elastic transfer processes is relevant [13,28,52]. In Fig. 8(a), the elastic scattering ( $\theta$ ) and elastic transfer ( $\pi-\theta$ ) angular distributions results are shown. From these results, one can say that the data corresponding to the backward angles are dominated by the forward angle transfer and, as a consequence, these data could be described by considering only the contribution of the transfer amplitude, i.e., without taking into account the interference effects. On the other hand, in the angular range around  $80^\circ \leq \theta \leq 120^\circ$ , the interference would be important and should be taken into account in the calculations. In Fig. 8(b), two results are shown. The solid

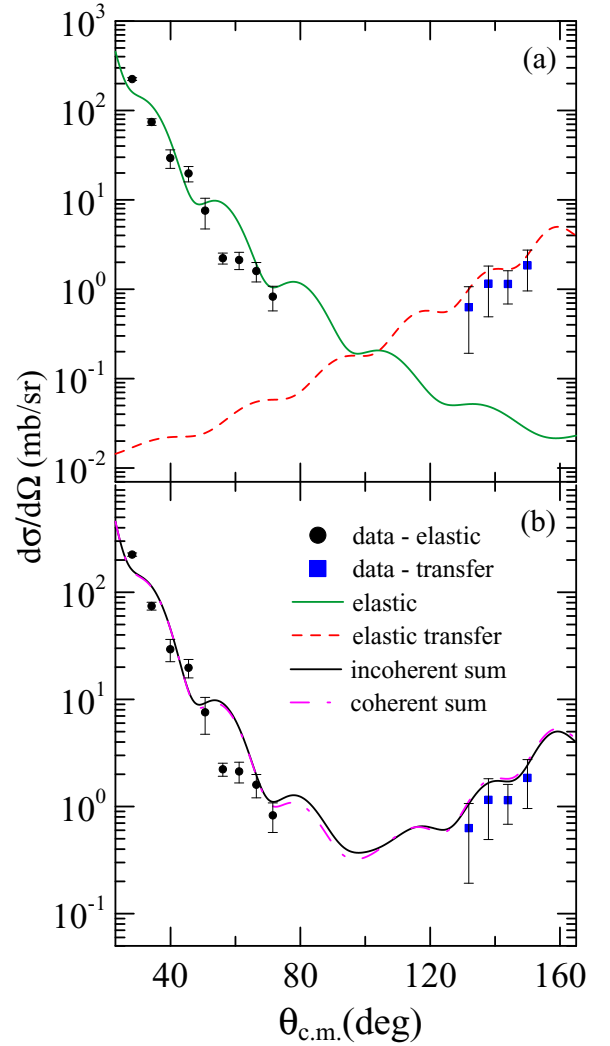


FIG. 8. CRC predictions for the angular distribution of the elastic scattering and elastic transfer processes, using the São Paulo potential in both partitions, compared to the experimental data.

black line is related to the sum of the elastic and transfer angular distributions without considering the interference effect, and the dashed-dot pink line is related to their coherent sum. Despite the slightly small differences in the angular distributions around the range of  $80^\circ \leq \theta \leq 120^\circ$ , the results are reasonably compatible outside this range. It is possible to extend this analysis for the  ${}^7\text{Be}_{0.43}({}^9\text{Be}_{\text{gs}}, {}^7\text{Be}_{0.43}){}^9\text{Be}_{\text{gs}}$  channel and to show that the most significant contribution to the angular distribution at backward angles comes from the inelastic transfer channel.

In particular, once the  ${}^7\text{Be}_{0.43}$  state cannot be resolved from the ground state because of the experimental energy resolution, it is important to assess the effect of the inelastic transfer at backward angles compared to the elastic transfer. If the orders of magnitude of both elastic and inelastic transfer are comparable, the measured angular distribution should be compared to the incoherent sum of the theoretical elastic and inelastic transfers as, in this case, the two channels are not identical.

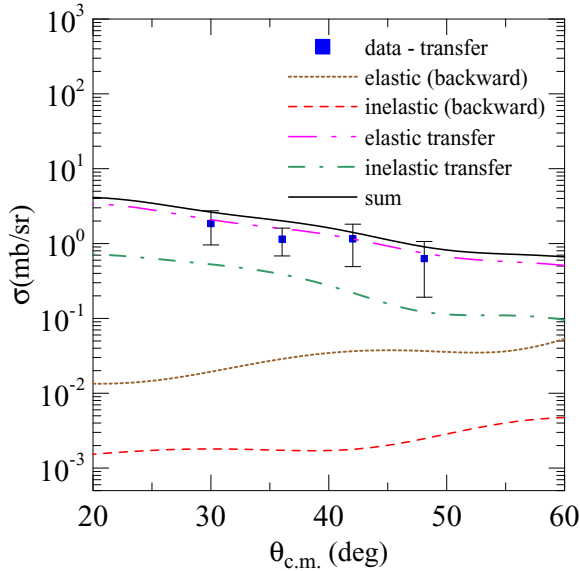


FIG. 9. Comparison of theoretical cross sections for different reaction channels, with the experimental transfer data.

In Fig. 9, a comparison between the experimental data, corresponding to the transfer channel, and the CRC results using independent coordinates model is shown. The solid curve includes a sum of all the possible contributions. As already mentioned, the data at backward angles mostly correspond to the forward angles transfer channel, and, therefore, this sum includes the transfer cross section where both residual nuclei,  ${}^7\text{Be}$  and the ejectile  ${}^9\text{Be}$ , remain in the ground state plus the inelastic transfer cross section, where the residual nuclei  ${}^7\text{Be}$  remains in the first excited  $1/2^-$  state (0.43 MeV) and the ejectile  ${}^9\text{Be}$  in the ground state. To verify the magnitude of the elastic and inelastic scattering in this energy range, where the transfer data were measured, the contribution of each specific channel (elastic, inelastic, elastic transfer, and inelastic transfer) is also shown in Fig. 9. One can notice that the elastic and inelastic transfer angular distribution has the most important contributions to describe the correct order of magnitude of the experimental data.

### B. CRC results using Woods-Saxon potentials: Comparison with DWBA results

An optical model (or one-channel, or potential scattering) analysis of the experimental elastic scattering angular distribution was also performed. The calculations were performed using the computer code FRESKO. We used Woods-Saxon form factors for both real and imaginary parts of the optical potential and varied all the six parameters (depths, reduced radii, and diffusenesses) to best reproduce the forward angle angular distribution. The derived parameters are shown in Table V, and the resulting fit is compared with the experimental data in Fig. 10. One sees that the data at forward angles (elastic) are very well reproduced. However, the optical model (OM) cross section at backward angles (not shown here) underestimates the data by at least three orders of magnitude and the OM

TABLE V. Woods-Saxon parameters obtained by fitting the elastic scattering angular distribution.

$V$ (MeV)	$r_{0r}$ (fm)	$a_{0r}$ (fm)	$W$ (MeV)	$r_{0i}$ (fm)	$a_{0i}$ (fm)	$\chi^2/N$
52(5)	1.11(7)	0.64(5)	12(2)	1.29(7)	1.04(5)	0.4

alone is not able to reproduce the observed cross section at backward angles.

To have a better insight in the influence of different optical potentials in the CRC results, we performed calculations with Woods-Saxon optical potential in the entrance and outgoing partitions, and compare with the results of the previous section using the São Paulo potential. The results are compared with the experimental data in Fig. 11 in the whole angle interval. One sees that although the WS potential reproduces very well the forward angles (elastic), it underestimates the backward angles cross section by almost one order of magnitude, even when the transfer is taken into account. The SPP, on the other hand, is not so good at forward angles but can account quite well for the cross section observed at backward angles (transfer).

As we have obtained a Woods-Saxon potential that describes the elastic scattering at forward angles, one should check the applicability of the distorted wave Born approximation (DWBA) to describe the experimental data. Besides, we can also analyze the effect caused by the potential choice and structural characteristics of the involved nuclei obtained from the shell-model calculations.

To do this, we removed the coupling with the inelastic state in entrance partition and performed DWBA calculation considering São Paulo and Woods-Saxon potential. We used the spectroscopic amplitudes from Table II. The results are shown in Fig. 12 where only the elastic scattering and elastic transfer are taken into account. In Fig. 12(a), one can observe a

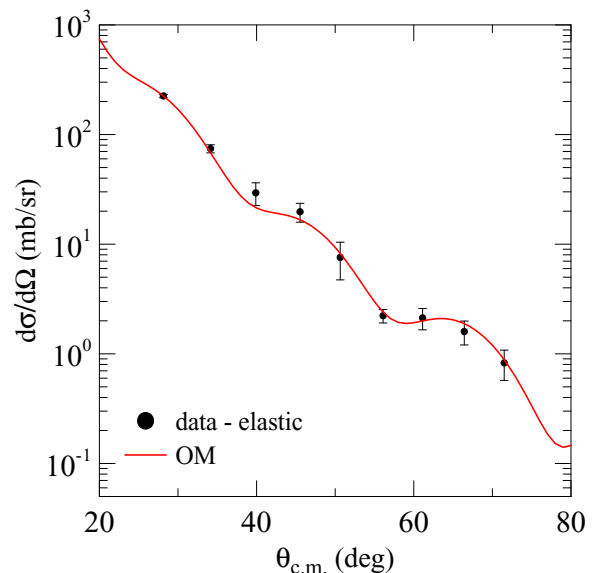


FIG. 10. Optical model fit of the elastic scattering angular distribution using Woods-Saxon form factors.

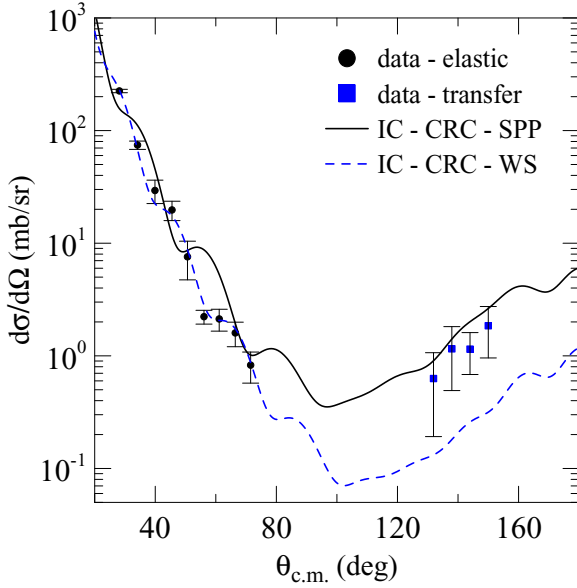


FIG. 11. Comparison between the experimental data and the theoretical results for elastic+transfer, by performing CRC calculations with different optical potentials.

better agreement between theoretical results and experimental data when the São Paulo potential is regarded, although the elastic scattering is not perfectly described. In principle, if the couplings with inelastic states are weak and the spectroscopic amplitudes related to projectile and target overlaps represent their correct structures, the DWBA approach should work, as soon as the elastic scattering is reasonably well described by the optical potential. Conversely, when one observes the Fig. 12(a), one realizes that the transfer data are not well described by considering Woods-Saxon potential in both ingoing and outgoing partitions even reproducing quite well the elastic scattering.

As a next step, we repeated our calculations with Woods-Saxon potential, changing the spectroscopic amplitudes to reproduce the data and then compare the derived amplitudes with the ones obtained from microscopic calculations. For the  $\langle {}^7\text{Be}_{\text{gs}}(3/2^-) | {}^9\text{Be}_{\text{gs}}(3/2^-) \rangle$  overlap, the more relevant structure contribution comes when the two neutrons are coupled to give  $J_{12} = 0$  or  $J_{12} = 2$  (see Table II). However, it is more likely to find the two neutrons transferred with  $J_{12} = 2$  than with  $J_{12} = 0$ , as it is shown in Fig. 12(b). In this figure, the dashed red curve is the result considering that the two transferred neutrons may be coupled to give  $J_{12} = 0$  or  $J_{12} = 2$  (DWBA-1), i.e.,

$$\begin{aligned} & \langle {}^7\text{Be}_{\text{gs}}(3/2^-) | {}^9\text{Be}_{\text{gs}}(3/2^-) \rangle \\ &= [-1.259|(1p_{3/2})^2\rangle_{J_{12}=2} - 0.035|(1p_{3/2}1p_{1/2})\rangle_{J_{12}=2}] \\ &+ [0.267|(1p_{3/2})^2\rangle_{J_{12}=0} + 0.174|(1p_{1/2})^2\rangle_{J_{12}=0}] \quad (3) \end{aligned}$$

with amplitudes given in Table II. The dash-dot-dot-dot cyan line represents the results when just  $J_{12} = 2$  is considered (DWBA-2), while the dashed-dashed-dot black line represents the results when only the other ( $J_{12} = 0$ ) component is taken

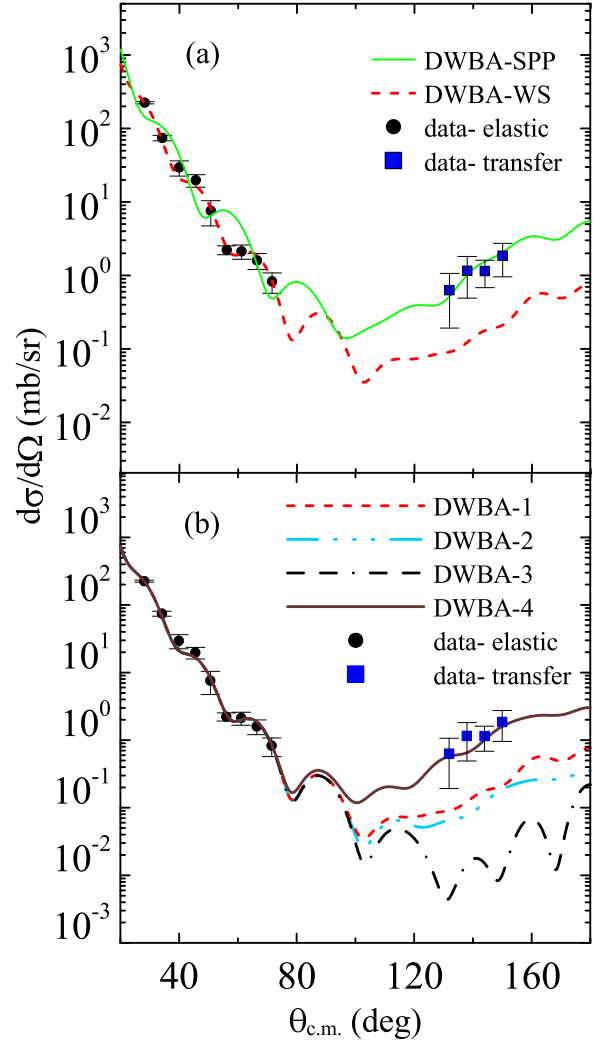


FIG. 12. Comparison of various DWBA results with the experimental data (see text for details).

into account (DWBA-3). Moreover, the most important component of the two-particle wave function is that when both neutrons are in  $1p_{3/2}$  orbit to give  $J_{12} = 2$ . For this reason, the spectroscopic amplitude of this component of the total wave function was varied to fit the data. The value found was 79% higher than that one derived from the shell-model calculation (DWBA-4), which represents a considerable disagreement between the amplitudes derived from the microscopic calculation and the DWBA approach.

The full dark-brown curve represents the result concerning the transfer cross section obtained by fitting the spectroscopic amplitude of the  $(1p_{3/2})^2$  two-neutron wave function component coupled to give  $J_{12} = 2$  with amplitudes  $SA = -2.259$ . The results of our DWBA calculations show that one has to be very careful deriving spectroscopic information from the fit of experimental data of transfer reaction through DWBA calculations, especially in the case of two-neutron transfer reaction, where different configurations can influence in the total wave function of the state.

### C. Angular smoothing

Due to the large angular acceptance of the detectors ( $\pm 3 \text{ deg}_{\text{lab}}$ ), beam spot size ( $\approx 4\text{--}5 \text{ mm}$  FWHM) and angular divergence of the secondary beam ( $1.5 \leq \theta \leq 4.5^\circ$ ), it is necessary to take into account the effect of the angular resolution in the theoretical angular distributions before comparison with the experimental data. This was done by calculating the folding of the angular distributions weighted by a normal distribution, around the central scattering angle and a width equal to the angular resolution of the experiment (see Eq. (4) of Ref. [53]). The angular resolution was determined by a Monte Carlo simulation of the scattering process taking into account the spot size and the angular divergence of the secondary beam, the acceptance of the detectors and the angular straggling in the target.

$$\frac{d\sigma}{d\Omega_{\text{conv}}} = \int_{\theta' - \Delta\theta}^{\theta' + \Delta\theta} \frac{d\sigma}{d\Omega_{\text{calc}}} G(\theta, \theta', \Delta\theta) d\theta, \quad (4)$$

where  $G(\theta, \theta', \Delta\theta)$  is the Gaussian distribution centered in  $\theta'$  and  $\Delta\theta$  is the standard deviation (angular acceptance). The results are illustrated in Fig. 13 where one can notice that the effect of the angular resolution is to smoothly reduce the amplitude of the oscillations of the angular distribution.

### IV. ${}^9\text{Be}(p, t){}^7\text{Be}$ REACTION

In the past,  $(p, t)$ ,  $(p, d)$ ,  $(d, t)$  transfer and other reactions have been extensively studied by considering  ${}^9\text{Be}$  as target nucleus to describe the elastic and inelastic scattering [54,55] as well as one-neutron [55–57] and two-neutron transfer [58] reactions. In particular, the  $(p, t)$  two-neutron transfer reaction was essential to probe the pairing correlation in transfer reactions.

In this section, we have selected the  ${}^9\text{Be}(p, t){}^7\text{Be}$  reaction for which there are excitation functions in the energy range from 14–23 MeV and  $p + {}^9\text{Be}$  elastic scattering angular distributions available to verify if the general features observed in this reaction are the same ones found by using  ${}^7\text{Be}$  as projectile. The details of the experimental procedure are given in Ref. [58].

The microscopic spectroscopic amplitudes corresponding to the couplings scheme for the target overlaps are the same of those used in the calculations of the previous section. On the other hand, it was considered the amplitude equal 1.0 for the  $\langle d|p \rangle$  and  $\langle t|p \rangle$  overlaps wave functions, while for the  $\langle t|d \rangle$  overlap the amplitude 1.22 [59] was used.

We carried out the two-neutron transfer calculations considering the São Paulo potential in the real part of the optical potential in the initial partition with strength coefficient  $N_r = 1.28$ . On the other hand, a Woods-Saxon potential was used in the imaginary part of the optical potential of this partition with geometric parameters  $V_w = 11.10 \text{ MeV}$ ,  $r_w = 1.06 \text{ fm}$  and  $a_w = 0.84 \text{ fm}$ . The spin-orbit interaction was also included with the following parameters  $V_{so} = 7.20 \text{ MeV}$ ,  $r_{so} = 1.30 \text{ fm}$ , and  $a_{so} = 0.70 \text{ fm}$ . Using this optical potential in the entrance partition, it was possible to reproduce the elastic scattering for the  $p + {}^9\text{Be}$  at 14.0, 15.0, and 21.35 MeV as one can observe in Fig. 14. For the outgoing partitions,

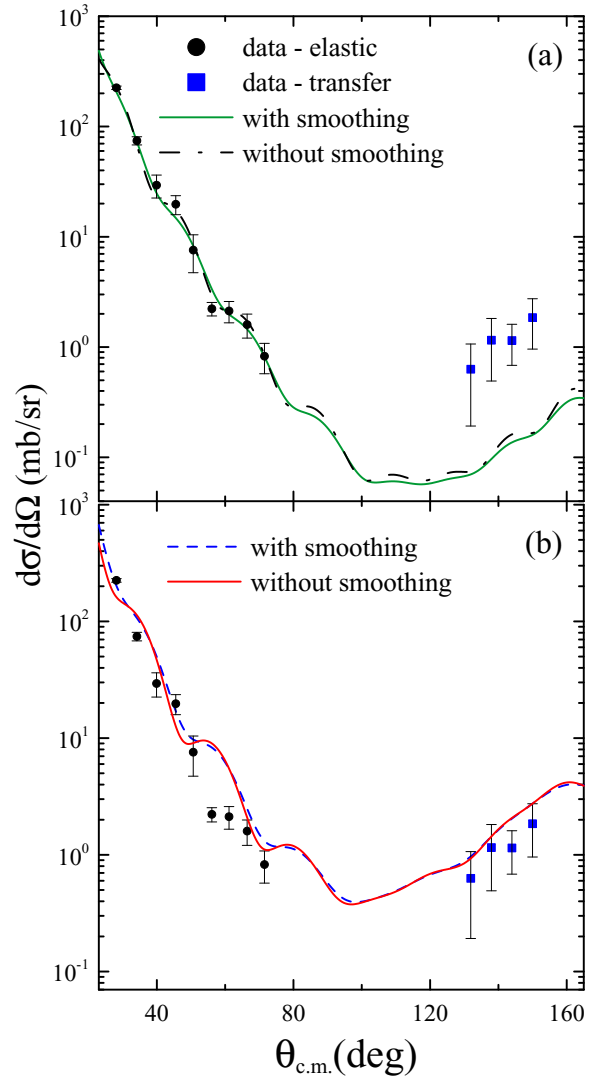


FIG. 13. Angular smoothing with (a) Woods-Saxon and (b) São Paulo potential in both partitions, respectively, using the CRC method.

the São Paulo potential was used in the real and imaginary parts with coefficient strength  $N_r = 1.0$  and  $N_i = 0.78$ . In Fig. 15, the results obtained for the two-neutron transfer cross sections in the energy interval from 14–23 MeV are shown in comparison with the experimental data. The integrated cross sections corresponding to the  $t + {}^7\text{Be}_{\text{gs}}$  channel (curves Seq-1 and IC-1), and the sum of both  $t + {}^7\text{Be}_{\text{gs}}$  and  $t + {}^7\text{Be}_{0.429}$  channels (curves Seq-2 and IC-2) were plotted in order to determine the effect of the  ${}^7\text{Be}_{0.429}$  state on the theoretical results. One observes that the effect of the inelastic transfer ( $t + {}^7\text{Be}_{0.429}$ ) is not so large.

The theoretical calculations concerning the two neutrons simultaneously transferred reproduce quite well the experimental data. Conversely, the results for the sequential process are lower than the measured cross sections by about one order of magnitude. These results are in agreement with those obtained in the previous subsections where it was shown that there is an indication that the two-neutron transfer in

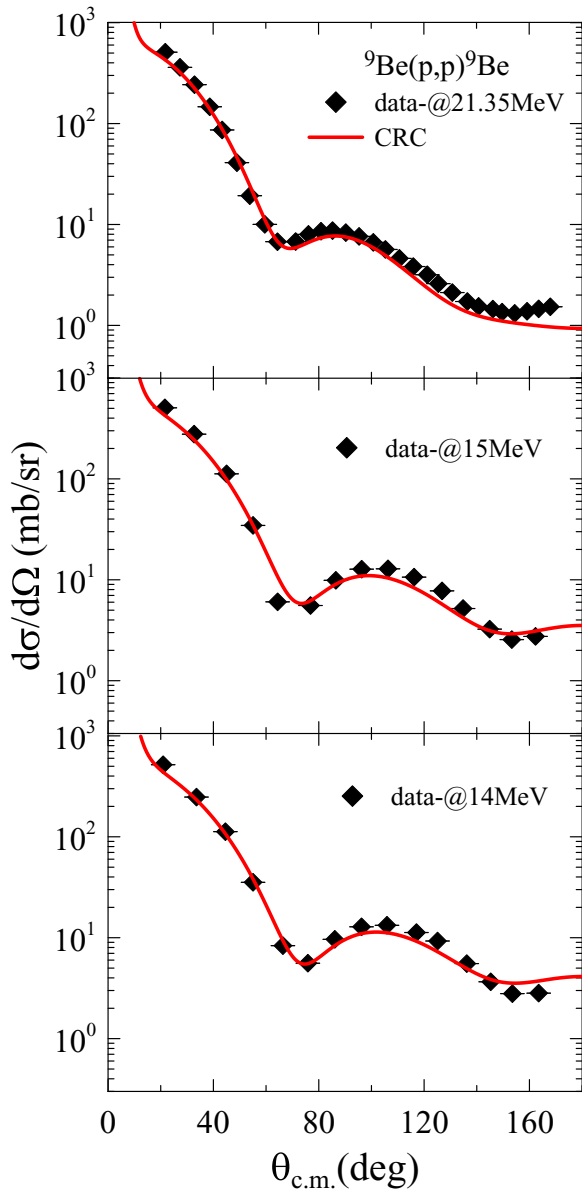


FIG. 14. Angular distribution for the  $p + {}^9\text{Be}$  elastic scattering at 14, 15, and 21.35 MeV incident energy.

the reaction ( ${}^9\text{Be}, {}^7\text{Be}$ ) are most likely to occur by a direct transfer process with both neutrons correlated. It is worth to mention that to consider two neutrons outside the core in transfer process with spectroscopic amplitudes derived by shell-model calculation, which appropriately describes the structures information of the nuclei involved in the reaction, has successfully described the angular distribution for the two-neutron transfer for many systems [13–21]. This indicate the feasibility of the method. On the other hand, as the cluster  $\alpha + \alpha + n$  configuration of  ${}^9\text{Be}$  target has not been considered in our structure calculations, our results are not completely exact in the absolute values, as the spectroscopic amplitudes of the ( ${}^7\text{Be}, {}^9\text{Be}$ ) overlap might be overestimated. As in our structure calculations the  ${}^4\text{He}$  has been chosen as a core, this means that one should take one neutron from the other

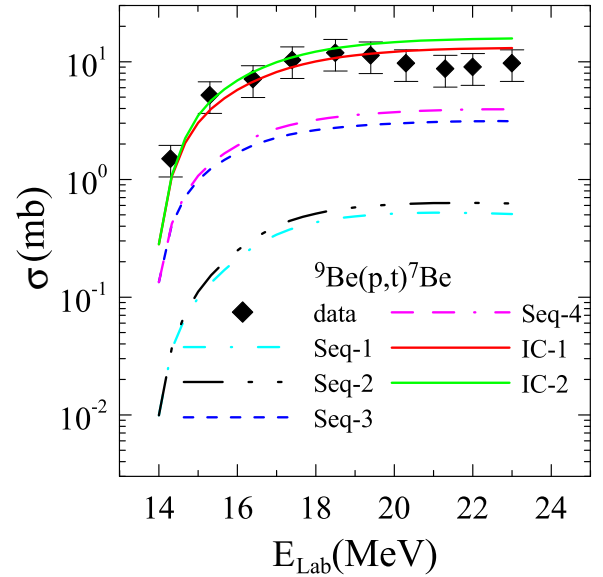


FIG. 15. Excitation function of the  ${}^9\text{Be}(p,t){}^7\text{Be}$  reaction in an incident energy range from 14–23 MeV.

$\alpha$  cluster (if the  $\alpha + \alpha + n$  configuration is considered as predominant) to transfer two neutrons. But the situation is the same for both sequential and direct transfer. This allows us to be confident, at least qualitatively, on our conclusion about the predominance of the direct (paired) two-neutron transfer reaction in these cases. The fact that we did not included the cluster structure of  ${}^9\text{Be}$  isotope could be the reason why we slightly over predicted the transfer cross section in Fig. 6.

Another important point is the relevance of the  ${}^8\text{Be}_{3.03}(2^+)$  state in the intermediate partition to describe the data by considering the sequential transfer. In Fig. 15, the Seq-1 and Seq-2 curves correspond to the results considering only the ground state of the  ${}^8\text{Be}$  in the intermediate partition while the Seq-3 and Seq-4 take into account both ground and  $3.03(2^+)$  excited state. It is clear the relevance of this intermediate  ${}^8\text{Be}_{3.03}(2^+)$  state once the cross sections increased almost one order of magnitude when it was considered. Although this was not explicitly shown in the case of the ( ${}^7\text{Be}, {}^9\text{Be}$ ) reaction, the inclusion of the  ${}^8\text{Be}_{3.03}(2^+)$  intermediate resonance was not so relevant for the sequential transfer in this last case.

## V. CONCLUSIONS

Elastic scattering and the transfer reaction for the  ${}^7\text{Be} + {}^9\text{Be}$  system have been measured at  $E_{\text{lab}} = 23.1$  MeV. The  ${}^7\text{Be}$  secondary beam has been produced in the RIBRAS facility at the University of São Paulo. The transfer reaction has been identified by detecting the  ${}^9\text{Be}$  at forward angles, which corresponds to the  ${}^7\text{Be}$  scattered at backward angles. The observed cross sections for  ${}^9\text{Be}$  were orders of magnitude larger than realistic optical model predictions indicating that processes other than pure elastic scattering are taking place at backward angles. The obvious candidate is the pickup from the target  ${}^9\text{Be}$  to the projectile  ${}^7\text{Be}$ . This transfer process leads to the same masses of the entrance channel and is called elastic transfer. Due to our limited experimental energy resolution,

the inelastic scattering and the transfer to the low-lying excited state in  ${}^7\text{Be}(1/2^-; 0.43 \text{ MeV})$  were also considered.

The transfer reactions have been analyzed in the context of the CRC method using the independent coordinates scheme. The spectroscopic amplitudes for each two-particle wave function component were microscopically calculated in the shell-model framework. Moreover, these structural calculations were able to describe reasonably well the known low-lying states, electric and magnetic quadrupole moment experimental data, as well as,  $B(E2)$  and  $B(M1)$  reduced transition probabilities for some transitions, giving confidence in our spectroscopic amplitudes. Nevertheless, our structure calculations did not account at all for the  $\alpha + \alpha + n$  configuration of the  ${}^9\text{Be}$  isotope. To include all these configurations in the same structure calculations is not an easy task at the moment.

It was shown that the magnitude of the backward angular distribution can be quite well reproduced considering the effect of the elastic transfer process. The effect of the elastic scattering and the inelastic excitations seem to be of minor importance at backward angles although the coupling with the inelastic excitation of the first excited state of the  ${}^7\text{Be}$  is important. The angular distribution was quite well described considering that both nucleons are simultaneously transferred, which suggests that the pairing correlation mentioned before is relevant for this process. The sequential transfer was considered and its effect is negligible in the whole angular range. As the  $\alpha$  clusters configuration of  ${}^9\text{Be}$  isotope was not considered, our results are approximate. Nevertheless, both direct and sequential transfers are expected to be affected in the same way by the missing cluster configurations, that, on the other hand, maybe the reason of the slight overestimation of the transfer data.

The same features have been observed in transfer calculations in the  ${}^9\text{Be}(p, t){}^7\text{Be}$  reaction, in which an available excitation function was quite well reproduced by considering the case where both valence neutrons are simultaneously transferred. Theoretical structure calculations also show that the two neutrons are preferably transferred to the  ${}^7\text{Be}_{\text{gs}}(3/2^-)$  state coupled to the  $J_{12} = 2$  total angular momentum of the two-neutron to generate the  ${}^9\text{Be}_{\text{gs}}(3/2^-)$  state. Moreover, in this transition, it is more likely to find both neutrons in

the  $1p_{3/2}$  orbit. The use of the same target overlaps to the elastic-transfer ( ${}^9\text{Be}, {}^7\text{Be}$ ) and  ${}^9\text{Be}(p, t){}^7\text{Be}$  reactions gave confidence in our form factors. In addition, it is to be noted that in the elastic-transfer case the analysis is simpler than in the  $(p, t)$  reaction, since the initial and final states are the same and the remnant terms are null.

Furthermore, we show that the choice a suitable optical potential is vital to describe both elastic and transfer channels studied in this work. Indeed, the CRC calculation has given good results for backward angles by using the double folding São Paulo potential in both ingoing and outgoing partitions. This choice makes the results utterly microscopic since the São Paulo potential is a parameter-free interaction, although the results at forward angles were not so good. The reason of this disagreement may be originated by the fact that we are taking into account the effect of breakup channels of both  ${}^7, {}^9\text{Be}$  nuclei by an effective imaginary potential (equal to the real part of the São Paulo potential with a strength factor  $N_I = 0.6$  in the entrance partition). Better results might be obtained if the breakup and the transfer channels would be considered in the same calculation, which would be extremely complicated in the present case in which the projectile breaks into two fragments and the target in three.

On the other hand, when a Woods-Saxon optical potential, which describes quite well the elastic scattering at forward angles was used in both partitions (instead of the double folding São Paulo potential), the transfer angular distribution was not well reproduced by the theoretical calculation as the result using the São Paulo potential. At backward angles, the difference between the theoretical and experimental angular distributions was less than one order of magnitude. With the aim to reproduce both elastic scattering and transfer angular distributions, the spectroscopic amplitudes of the most relevant wave function component should be increased by about 80%, and this might not reveal the actual structure of the nuclei.

## ACKNOWLEDGMENTS

The authors acknowledge partial financial support from CNPq, FAPERJ, FAPESP procs. No. 2013/22100-7, No. 2016/21434-7, CAPES, and INCT-FNA (Instituto Nacional de Ciência e Tecnologia- Física Nuclear e Aplicações).

- 
- [1] W. Von Oertzen and A. Vitturi, *Rep. Prog. Phys.* **64**, 1247 (2001).
  - [2] W. von Oertzen and H. G. Bohlen, *Phys. Rep.* **19**, 1 (1975).
  - [3] R. A. Broglia, *Ann. Phys. (NY)* **80**, 60 (1973).
  - [4] M. Assunção, R. Lichtenthäler, V. Guimarães, A. Lépine-Szily, G. F. Lima, and A. M. Moro, *Phys. Rev. C* **70**, 054601 (2004).
  - [5] P. Guazzoni *et al.*, *Phys. Rev. C* **83**, 044614 (2011).
  - [6] M. S. Golovkov *et al.*, *Phys. Rev. C* **72**, 064612 (2005).
  - [7] S. Mordechai, H. T. Fortune, G. E. Moore, M. E. Cobern, R. V. Kollarits, and R. Middleton, *Nucl. Phys. A* **301**, 463 (1978).
  - [8] A. M. Baxter and S. Hinds, *Nucl. Phys. A* **211**, 7 (1973).
  - [9] W. P. Alford, J. A. Cameron, E. Habib, and B. H. Wildenthal, *Nucl. Phys. A* **454**, 189 (1986).
  - [10] W. P. Alford, R. N. Boyd, E. Sugarbaker, D. L. Hanson, and E. R. Flynn, *Phys. Rev. C* **21**, 1203 (1980).
  - [11] M. E. Cobern, L. C. Bland, H. T. Fortune, G. E. Moore, S. Mordechai, and R. Middleton, *Phys. Rev. C* **23**, 2387 (1981).
  - [12] M. Igarashi, K. Kubo, and K. Yagi, *Phys. Rep.* **199**, 1 (1991).
  - [13] M. J. Ermamatov *et al.*, *Phys. Rev. C* **94**, 024610 (2016).
  - [14] M. Cavallaro, F. Cappuzzello, M. Bondi, D. Carbone, V. N. Garcia, A. Gargano, S. M. Lenzi, J. Lubian, C. Agodi, F. Azaiez *et al.*, *Phys. Rev. C* **88**, 054601 (2013).
  - [15] M. Cavallaro, C. Agodi, M. Assié, F. Azaiez, F. Cappuzzello, D. Carbone, N. de Séréville, A. Foti, L. Pandola, J. A. Scarpaci *et al.*, *Phys. Rev. C* **93**, 064323 (2016).

- [16] D. Carbone, F. Cappuzzello, M. Cavallaro, A. Cunsolo, A. Foti, S. Tudisco, M. Bondi, G. Santagati, G. Taranto, R. Chen *et al.*, *J. Phys.: Conf. Ser.* **312**, 082016 (2011).
- [17] F. Cappuzzello, D. Carbone, M. Cavallaro, M. Bondi, C. Agodi, F. Azaiez, A. Bonaccorso, A. Cunsolo, L. Fortunato, A. Foti *et al.*, *Nature Commun.* **6**, 6743 (2015).
- [18] M. J. Ermamatov, R. Linares, J. Lubian, J. L. Ferreira, F. Cappuzzello, D. Carbone, M. Cavallaro, M. Cubero, P. N. de Faria, A. Foti, G. Santagati, and V. A. B. Zagatto, *Phys. Rev. C* **96**, 044603 (2017).
- [19] D. Carbone, J. L. Ferreira, F. Cappuzzello, J. Lubian, C. Agodi, M. Cavallaro, A. Foti, A. Gargano, S. M. Lenzi, R. Linares, and G. Santagati, *Phys. Rev. C* **95**, 034603 (2017).
- [20] B. Paes, G. Santagati, R. M. Vsevolodovna, F. Cappuzzello, D. Carbone, E. N. Cardozo, M. Cavallaro, H. García-Tecocoatzi, A. Gargano, J. L. Ferreira, S. M. Lenzi, R. Linares, E. Santopinto, A. Vitturi, and J. Lubian, *Phys. Rev. C* **96**, 044612 (2017).
- [21] E. N. Cardozo, J. Lubian, R. Linares, F. Cappuzzello, D. Carbone, M. Cavallaro, J. L. Ferreira, A. Gargano, B. Paes, and G. Santagati, *Phys. Rev. C* **97**, 064611 (2018).
- [22] M. Bernas, M. Roy-Stephan, F. Pougheon, M. Langevin, G. Rotbard, P. Roussel, J. P. LeFèvre, M. C. Lemaire, K. S. Low, and B. H. Wildenthal, *Phys. Rev. C* **19**, 2246 (1979).
- [23] M. C. Lemaire and K. S. Low, *Phys. Rev. C* **16**, 183 (1977).
- [24] A. Parmar, Sonika, B. J. Roy, V. Jha, U. K. Pal, T. Sinha, S. K. Pandit, V. V. Parkar, K. Ramachandran, K. Mahata, S. Santra, and A. K. Mohanty, *Nucl. Phys. A* **940**, 167 (2015).
- [25] I. Tanihata *et al.*, *Phys. Rev. Lett.* **100**, 192502 (2008).
- [26] M. C. Morais and R. Lichtenthäler, *Nucl. Phys. A* **857**, 1 (2011).
- [27] A. Lépine-Szily, M. S. Hussein, R. Lichtenthäler, J. Cseh, and G. Lévai, *Phys. Rev. Lett.* **82**, 3972 (1999).
- [28] A. Vitturi and C. H. Dasso, *Nucl. Phys. A* **458**, 157 (1986).
- [29] R. Lichtenthäler, A. Lépine-Szily, V. Guimarães *et al.*, *Eur. Phys. J. A* **25**, 733 (2005).
- [30] A. Lépine-Szily, R. Lichtenthäler, and V. Guimarães, *Eur. Phys. J. A* **50**, 128 (2014).
- [31] I. J. Thompson, <http://www.fresco.org.uk>
- [32] L. C. Chamon, D. Pereira, M. S. Hussein, M. A. Cândido Ribeiro, and D. Galetti, *Phys. Rev. Lett.* **79**, 5218 (1997).
- [33] D. Pereira, J. Lubian, J. R. B. Oliveira, D. P. de Souza, and L. C. Chamon, *Phys. Lett. B* **670**, 330 (2009).
- [34] Y. Sakuragi, M. Yahiro, and M. Kamimura, *Prog. Theor. Phys.* **70**, 1047 (1983).
- [35] L. F. Canto, P. R. S. Gomes, R. Donangelo, and M. S. Hussein, *Phys. Rep.* **424**, 1 (2006).
- [36] L. F. Canto, P. R. S. Gomes, R. Donangelo, J. Lubian, and M. S. Hussein, *Phys. Rep.* **596**, 1 (2015).
- [37] J. P. Fernández-García *et al.*, *Phys. Rev. C* **92**, 044608 (2015).
- [38] A. M. Moro, K. Rusek, J. M. Arias, J. Gómez-Camacho, and M. Rodríguez-Gallardo, *Phys. Rev. C* **75**, 064607 (2007).
- [39] D. P. Souza, D. Pereira, J. Lubian, L. C. Chamon, J. R. B. Oliveira, E. S. Rossi Jr., C. P. Silva, P. N. de Faria, V. Guimarães, R. Lichtenthäler, and M. A. G. Alvarez, *Nucl. Phys. A* **836**, 1 (2010).
- [40] L. R. Gasques, L. C. Chamon, P. R. S. Gomes, and J. Lubian, *Nucl. Phys. A* **764**, 135 (2006).
- [41] A. T. Rudchik, K. W. Kemper, V. O. Romanyshyn, O. A. Ponkratenko, V. M. Kyryanchuk, and V. V. Uleshchenko, *Eur. Phys. J. A* **41**, 31 (2009).
- [42] G. R. Satchler, *Direct Nuclear Reactions* (Oxford University Press, New York, 1983).
- [43] V. Della Rocca and F. Iachello, *Nucl. Phys. A* **973**, 1 (2018).
- [44] V. Della Rocca, R. Bijker, and F. Iachello, *Nucl. Phys. A* **966**, 158 (2017).
- [45] NUSHELLX for Windows and Linux, <http://www.garsington.eclipse.co.uk/>
- [46] Y. Utsuno and S. Chiba, *Phys. Rev. C* **83**, 021301(R) (2011).
- [47] F. Ajzenberg-Selove, *Nucl. Phys. A* **490**, 1 (1988).
- [48] J. Hiura and R. Tamagaki, *Prog. Theor. Phys. Suppl.* **52**, 25 (1972).
- [49] B. A. Urazbekova, A. S. Denikina, S. K. Sakhiev, and N. T. Burtebaev, *Bull. Russ. Acad. Sci.* **80**, 247 (2016).
- [50] V. T. Voronchev, V. I. Kukulin, V. N. Pomerantsev, and G. G. Ryzhikh, *Few-Body Syst.* **18**, 191 (1995).
- [51] R. M. DeVries, *Nucl. Phys. A* **212**, 207 (1973).
- [52] J. Christley, M. Nagarajan, and A. Vitturi, *Nucl. Phys. A* **591**, 341 (1995).
- [53] K. C. C. Pires, R. Lichtenthäler, A. Lépine-Szily, and V. Morcelle, *Phys. Rev. C* **90**, 027605 (2014).
- [54] F. S. Mozer, *Phys. Rev.* **104**, 1386 (1956).
- [55] S. E. Darden, G. Murillo, and S. Sen, *Nucl. Phys. A* **266**, 29 (1976).
- [56] D. De Jong, P. M. Endt, and L. J. G. Simons, *Physica* **18**, 676 (1952).
- [57] J. A. Biggerstaff, R. F. Hood, H. Scott, and M. T. McEllistrem, *Nucl. Phys.* **36**, 631 (1962).
- [58] B. I. Cohen and T. H. Handley, *Phys. Rev.* **93**, 514 (1954).
- [59] N. Burtebayev *et al.*, *Acta Phys. Pol. B* **46**, 1037 (2015).